ROYAL SOCIETY
OF **CHEMISTRY**

ICM
Industrial Chemistry & Materials

ROYAL SOCIETY
OF CHEMISTRY

PAPER

Check for updates

Hybrid alkyl-ligand tin-oxo clusters for enhanced lithographic patterning performance *via* intramolecular interactions†

Hao Chen,‡[a] Wenzheng Li,‡[a] Yingdong Zhao,[a] Xinyan Huang,[a] Jialong Zhang,*[b] Peijun Ji,[b] Jun Zhao,[c] Pengzhong Chen iD *[a] and Xiaojun Peng iD *[ad]

Tin-oxo clusters (TOCs) are promising candidates for next-generation extreme ultraviolet (EUV) photoresist materials due to their strong EUV absorption properties and small molecular sizes. The surface ligands are critical to the photolithographic patterning process; however, the precise regulatory mechanisms governing their functionality require further investigation. Building upon our previously reported Sn4-oxo clusters, Sn4-Me–C10 and Sn4-Bu–C10, which incorporate butyl and methyl groups, respectively, this study presents the synthesis of a novel cluster, **Sn4-MB**, which integrates both butyl and methyl groups within the same Sn4-oxo core. This new compound demonstrates superior patterning performance compared to both Sn4-Me–C10 and Sn4-Bu–C10, as well as their mixed formulations. The enhanced performance is attributed to the intramolecular hybridization between Sn–methyl and Sn–butyl moieties in **Sn4-MB**, which facilitates radical feedback regulation, thereby minimizing energy dissipation and suppressing the extent of reaction diffusion during pattern formation. In electron beam lithography (EBL) exposure experiments, optimization of the developer and reduction of film thickness allowed **Sn4-MB** to achieve lines with a critical dimension (CD) of 17 nm. Furthermore, during EUV exposure, **Sn4-MB** produced 75 nm pitch lines at a dose of 150 mJ cm^{-2}, with a line CD of 33 nm. This study provides an effective molecular design strategy for enhancing the lithographic performance of TOC photoresists, highlighting their substantial potential for next-generation EUV lithography applications.

Keywords: Tin-oxo clusters; Intramolecular radical regulation; Photoresist; Electron beam lithography; Extreme ultraviolet lithography.

1 Introduction

The photolithography process is a fundamental technology in semiconductor manufacturing, with photoresists serving as the most critical and essential material.[1–5] Over the past several decades, modifications to the structure and formulation of photoresists have been continuously implemented to align with

[a] *State Key Laboratory of Fine Chemicals, Frontiers Science Center for Smart Materials, School of Chemical Engineering, Dalian University of Technology, Dalian 116024, China. E-mail: pengxj@dlut.edu.cn, pzchen@dlut.edu.cn*

[b] *Sinopec Shanghai Research Institute of Petrochemical Technology Co., Ltd., Shanghai 201208, China. E-mail: zhangjialong.sshy@sinopec.com*

[c] *Shanghai Advanced Research Institute, Chinese Academy of Sciences, Shanghai 201203, China*

[d] *State Key Laboratory of Fine Chemicals, College of Materials Science and Engineering, Shenzhen University, Shenzhen 518060, China*

† Electronic supplementary information (ESI) available: CCDC 2443045. For ESI and crystallographic data in CIF or other electronic format see DOI: https://doi.org/10.1039/d5im00058k

‡ These authors contributed equally to this work.

the ongoing reduction in the exposure wavelength of light sources.[6–13] These advancements have contributed to the enhanced resolution of periodic patterns in the photolithography process. Extreme ultraviolet (EUV) lithography has emerged as a pivotal technique for achieving process nodes below 7 nm in integrated circuits by utilizing a 13.5 nm exposure wavelength.[14–17] With the introduction of high numerical aperture (NA) EUV equipment, metal oxide resists (MORs) have been officially designated as the specialized photoresist architecture to replace conventional polymer photoresists.[18,19] Consequently, the design and development of novel MORs,[20–24] along with investigations into the relationship between their structures and exposure mechanisms, are essential for advancing their practical application in the lithography process.[25–29]

MORs offer many advantages, including significant EUV absorption by the central metal atoms, a reduced molecular size, and enhanced etch resistance.[21,30–32] These characteristics facilitate the fabrication of thinner films that exhibit a lower susceptibility to pattern collapse. The surface organic ligands

© 2025 The Author(s). Co-published by the Institute of Process Engineering, Chinese Academy of Sciences and the Royal Society of Chemistry

Ind. Chem. Mater., 2025, **3**, 543–552 | **543**

significantly influence the dispersion and stability of the MOR in organic solvents, as well as its film-forming capability.[25,27,33] More critically, these ligands play a crucial role in the photolithography reaction process.[34–40] Upon the absorption of EUV photons (92 eV), the MOR generates high-energy photoelectrons with an approximate energy of 80 eV, which subsequently induces ionization within the resist, resulting in the generation of secondary electrons.[4,41–43] This cascade of secondary electrons leads to the departure or dissociation of ligands through the cleavage of metal–oxygen or metal–carbon bonds.[28,44,45] Following this, condensation and coupling reactions occur within the inner core, ultimately forming a metal-oxide network structure that exhibits altered solubility compared to the pre-exposure materials.[20,37] This process operates *via* a free radical mechanism, and the structural properties of organic ligands significantly influence the efficiency of radical generation and the extent of reaction diffusion, which are critical to the resolution and sensitivity of the resulting patterns.

Our prior investigation into two tin-oxo clusters,[35] Sn4–Me–C10 and Sn4–Bu–C10, which possess an identical SnO inner core but are capped with methyl and butyl groups, respectively, has revealed that the properties of organic ligands significantly affect patterning performance (Scheme 1). The Sn4–Bu–C10 cluster, characterized by relatively low Sn–butyl bond strengths, exhibits increased sensitivity; however, it generates butyl radicals that lead to extensive reaction diffusion during radiation exposure, thereby compromising resolution. In contrast, the Sn4–Me–C10 cluster generates methyl radicals that induce relatively limited reaction diffusion, resulting in high-resolution patterns, albeit at the cost of requiring higher radiation doses. These findings prompted us to explore the integration of butyl and methyl ligands within mixed Sn-oxo clusters. The

intermolecular coexistence of both radical types facilitates feedback regulation, thereby suppressing the extent of reaction diffusion and enabling simultaneous improvements in resolution and sensitivity.[34] Nevertheless, the stability and thermal reliability of these hybrid photoresists were found to be insufficient, and due to the slow interaction efficiency between the two clusters, their patterning capabilities still necessitate further enhancement to meet the stringent requirements of advanced EUV lithography.

In this study, we report a novel Sn-oxo cluster, **Sn4-MB**, which contains both Sn–methyl and Sn–butyl groups, aiming to achieve synergistic regulation of resolution and sensitivity by modifying the pathways of radical generation and the extent of reaction diffusion. The presence of methyl and butyl free radicals generated within the molecule facilitates intramolecular interactions that reduce energy transfer losses and suppress the extent of reaction diffusion. Compared to the hybrid formulation, **Sn4-MB** demonstrates a significant improvement in patterning performance. By optimizing the developer and reducing the photoresist film thickness, **Sn4-MB** achieved periodic lines with a CD of 17 nm. Additionally, **Sn4-MB** produced a line CD of 33 nm in line/space (L/S) patterns with a pitch of 75 nm at a dose of 150 mJ cm^{-2} under EUV exposure, indicating its substantial potential for application in EUV lithography.

2 Results and discussion

The synthesis procedure for **Sn4-MB** is detailed in the ESI† and its structure is characterized using ^{1}H NMR, ^{13}C NMR (Fig. S1 and S2†), and single crystal X-ray diffraction analysis. The molecular structure of **Sn4-MB** is centered around a crystallographic inversion point, with an approximate size of 1.8 nm (Fig. 1a). This structure is organized around a central
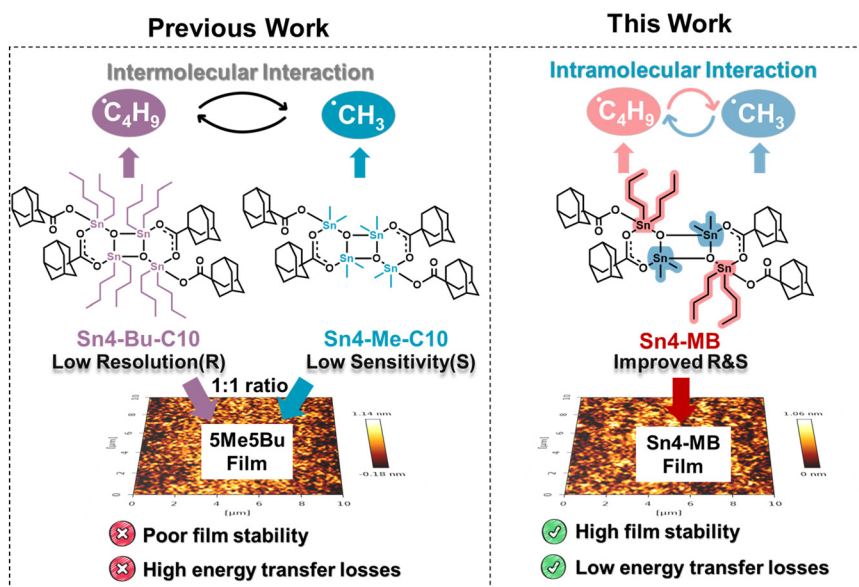
Scheme 1 Schematic representation of intramolecular interactions during exposure of the hybrid alkyl ligand tin-oxo cluster photoresist **Sn4-MB**.
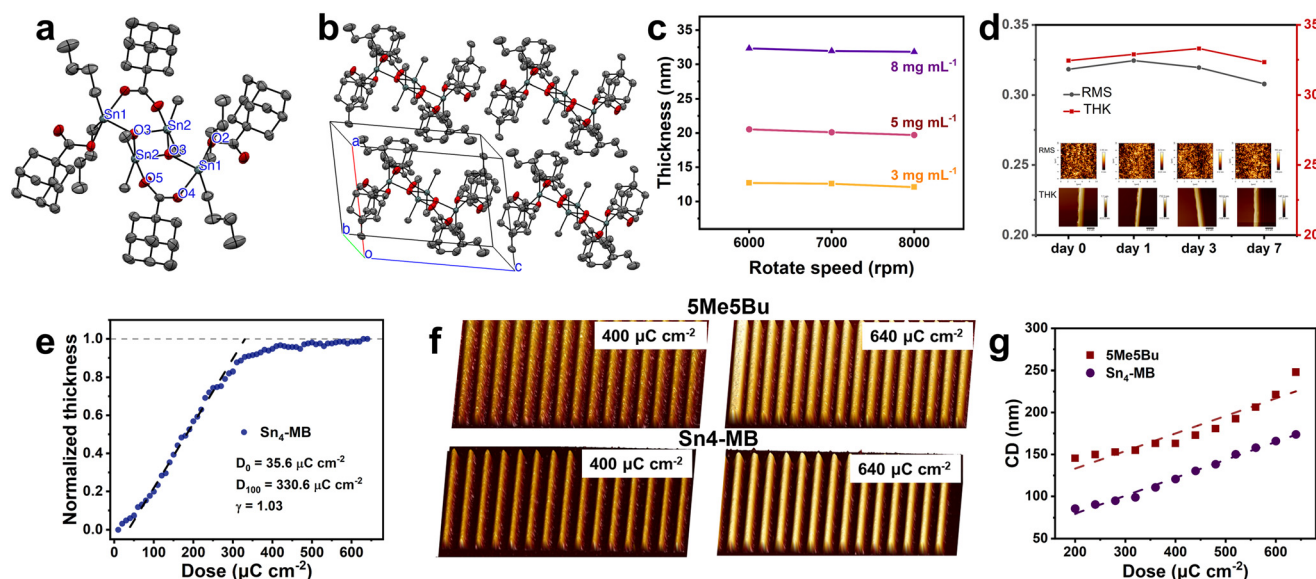
Fig. 1 (a) and (b) Single crystal structures of **Sn4-MB**. The hydrogen atoms were omitted for clarity; (c) thickness of films obtained from different concentrations of **Sn4-MB** precursor solutions at different rotational speeds; (d) time-dependent variation in surface roughness (RMS) and film thickness (THK) of **Sn4-MB** films at days 0, 1, 3, and 7 after spin-coating. Insets show AFM surface topography (top row) and cross-sectional profiles (bottom row), corresponding to the same time points from left to right; (e) contrast curves of **Sn4-MB**; (f) AFM images of L/3S dense line patterns (100 nm pitch) generated from **Sn4-MB** and **5Me5Bu** resists under area-exposure at electron beam doses of 400 and 640 $\mu C\ cm^{-2}$; (g) periodic line CD of **Sn4-MB** and **5Me5Bu** films under area-exposure as a function of exposure dose.

Sn_2O_2 core, which includes endocyclic Sn2 atoms linked to two exocyclic Sn1 atoms. The O3 atom functions as a μ_3-oxo ligand. The bond lengths of Sn2–O3 and Sn2–O3^i within the core are measured at 2.153 Å and 2.042 Å, respectively, both of which are longer than the Sn1–O3 bond length of 2.031 Å. A bidentate bridging adamantane carboxylic acid further connects the exocyclic and endocyclic Sn atoms, with bond lengths of Sn1–O4 at 2.266 Å and Sn2^i–O5 at 2.250 Å, indicating a nearly symmetric bridge. Additionally, the remaining adamantane carboxylic acid coordinates to the exocyclic Sn1 atom in a monodentate fashion, with a Sn1–O2 bond length of 2.177 Å. Furthermore, the endocyclic Sn2 and exocyclic Sn1 atoms are orthogonally aligned with two methyl groups and two butyl groups, respectively. The measured bond lengths for the Sn–butyl interactions are 2.131 Å and 2.148 Å, which are longer than the Sn–methyl bond lengths of 2.105 Å and 2.121 Å, suggesting a variation in the dissociation energy of these Sn–C bonds. The overall molecular structure demonstrates steric hindrance effects due to the presence of two orthogonally positioned butyl groups, which occupy spaces above and below the central SnO plane. This arrangement hinders close intermolecular packing and interactions, thereby facilitating the formation of high-quality films and high-resolution patterns (Fig. 1b).

The **Sn4-MB** films were fabricated using a spin-coating technique on a polished substrate measuring 1 cm × 1 cm. The thickness of the film prepared from a **Sn4-MB** solution at a concentration of 8 mg mL^{-1} was measured as 32.3 nm when spin-coated at a speed of 6000 rpm. Under identical conditions, the thickness decreased to 20.5 nm and 12.7 nm for concentrations of 5 mg mL^{-1} and 3 mg mL^{-1}, respectively

(Fig. 1c and S3†). The production of thinner films aligns with the requirements of high-numerical aperture (NA) EUV lithography,[46] where a reduced depth of focus (DoF) must be taken into account. Additionally, varying the spin-coating speed from 6000 to 8000 rpm resulted in negligible changes in film thickness across the different concentrations tested. Fig. 1d shows the time-dependent variation in surface roughness (RMS) and film thickness (THK) of **Sn4-MB** films over a 7 day period after spin-coating. These data indicate that the film remains morphologically stable, with minimal changes in thickness and surface roughness over time.

2.1 Contrast curve and patterned periodic lines

The analysis of the contrast curve revealed that **Sn4-MB** exhibited a D_0 value of 35.6 $\mu C\ cm^{-2}$, a D_{100} value of 330.6 $\mu C\ cm^{-2}$, and a contrast (γ) of 1.03 (Fig. 1e). Subsequently, the patterning performance of **Sn4-MB** was further conducted and compared with that of the hybrid photoresist formulation **5Me5Bu**, which consists of a physical mixture of Sn–Bu–C10 and Sn–Me–C10 in an equivalent ratio (Scheme 1). In area-EBL experiments conducted under identical conditions, the critical dimension (CD) of the periodic lines produced by **Sn4-MB** was significantly narrower than that of **5Me5Bu** (Fig. S4 and S5†). For instance, at an exposure dose of 400 $\mu C\ cm^{-2}$, **Sn4-MB** and **5Me5Bu** yielded pattern lines with corresponding CDs of 121 nm and 173 nm, respectively, and at 640 $\mu C\ cm^{-2}$, the CDs were 174 nm and 248 nm, respectively (Fig. 1f). The variation in line CDs with respect to exposure dose for **Sn4-MB** demonstrated an enhancement when compared to **5Me5Bu** (Fig. 1g).

Additionally, the line edge roughness (LER) for **Sn4-MB** also showed improvement. In the line EBL experiment, the line CD was markedly reduced from 71.2 nm for **5Me5Bu** to 34.1 nm for **Sn4-MB** at a dose of 24.5 nC cm^{-1} (Fig. S6–S9†).

Overall, the patterning properties of **Sn4-MB** have been significantly and comprehensively enhanced in comparison to the previously reported **5Me5Bu** hybrid alkyl ligand photoresists, particularly regarding sensitivity, resolution, and LER. This enhancement can be attributed not only to the reduced bond energy of the Sn–C bond in **Sn4-MB** relative to Sn4–Me–C10 and Sn4–Bu–C10 (Fig. S10†), but also to the direct feedback regulation occurring within the molecule due to the Sn–methyl and Sn–butyl bonds, as well as the radicals generated in **Sn4-MB**. This intramolecular interaction minimizes energy transfer losses and suppresses the extent of reaction diffusion. Consequently, the improved efficiency of energy utilization and radical confinement has optimized the patterning performance of **Sn4-MB**.

When the line period was reduced, the **Sn4-MB** photoresist in the unexposed regions was inadequately removed by the IPA:DIW solution at a 3:1 ratio, resulting in residual material remaining on the silicon substrate after the development process. This residue subsequently impeded the pattern transfer process. Thus, the selection of an appropriate developer is critical for improving resolution and sensitivity. Subsequently, EA:IPA solution at a 3:1 ratio was selected as the developer, leading to **Sn4-MB** films producing lines with a pitch of 100 nm, achieving a critical dimension (CD) of 24.1 nm and a line edge roughness (LER) of 4.93 nm at an exposure dose of 26 nC cm^{-1} (Fig. 2a and S11†). Under identical exposure and development conditions, **Sn4-MB** yielded lines with a CD of 23.6 nm and a LER of 4.40 nm when utilizing a 70 nm period line template (Fig. 2b and S12†). Conversely, the CD of lines developed solely with EA was measured at 32.1 nm (Fig. 2c, S13 and S14†). The introduction of new developers not only effectively removed the **Sn4-MB** photoresist from the unexposed areas but also resulted in narrower periodic lines. The CD and LER of lines developed with the EA:IPA solution at a 3:1 ratio was smaller compared to those developed with EA alone, and exhibited a more gradual variation with respect to the exposure dose (Fig. 2d and e). Consequently, the Z constant[47] of the lines was reduced when developed with the EA:IPA solution at a 3:1 ratio compared to development with EA, as illustrated in Fig. 2f. Although the CD and LER of the periodic lines were superior when developed with EA:IPA at a 3:1 ratio, the height of the lines produced through EA development was marginally greater, which may facilitate subsequent pattern transfer (Fig. 2g, h, and S15†).
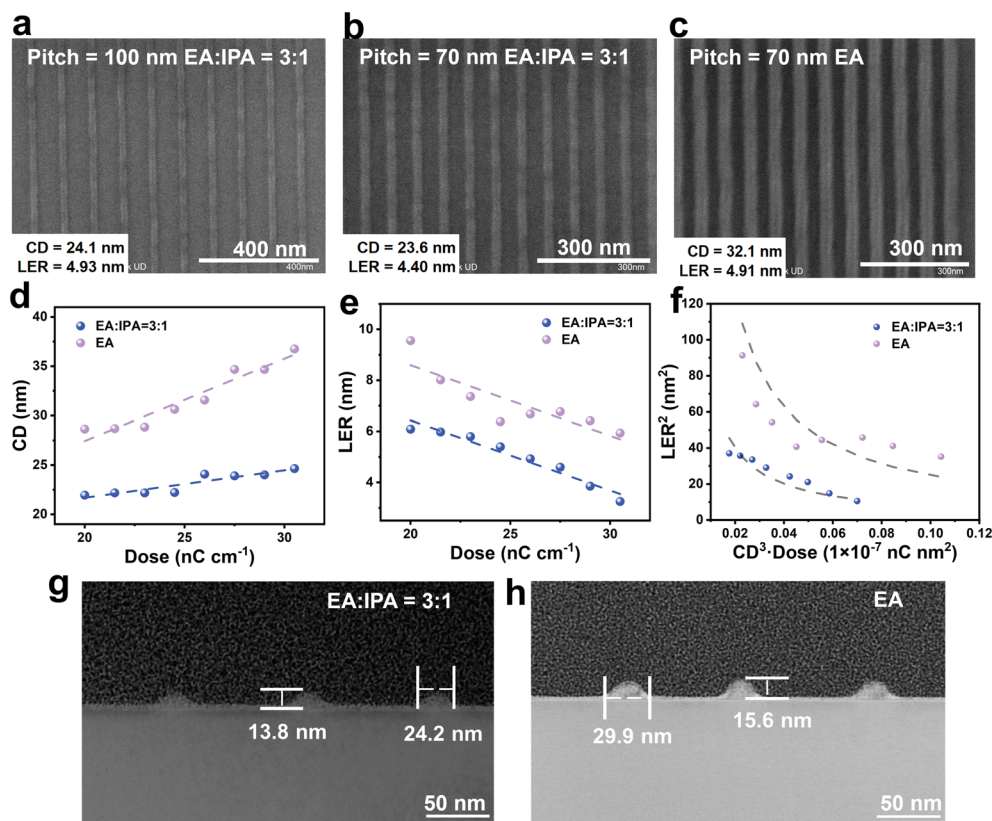

Fig. 2 SEM images of the **Sn4-MB**'s (a) 100 nm and (b) 70 nm pitch lines when developed with EA:IPA = 3:1 at 26 nC cm^{-1} exposure doses; (c) SEM image of the **Sn4-MB**'s 70 nm pitch lines when developed with EA at 26 nC cm^{-1} exposure dose; relation of 100 nm pitch line (d) CD and (e) LER with dose after EA:IPA = 3:1 and EA development of **Sn4-MB** films upon EBL line-exposure; (f) Z constant of **Sn4-MB**'s 100 nm pitch lines under EA:IPA = 3:1 and EA development; profile of **Sn4-MB**'s lines when developed with (g) EA:IPA = 3:1 and (h) EA.

EBL experiments were further conducted at a lower voltage of 10 kV. Compared to the 30 kV condition, the 10 kV reduces the electron penetration depth while increases the energy deposition per unit distance, thereby enabling more efficient exposure and lowering the required dose. By utilizing EA development, 70 nm pitch lines with a CD of 24.3 nm were produced at a minimum dose of 8 nC cm^{-1} (Fig. S16†). In contrast, the use of EA : IPA for development yielded lines with a CD 19.1 nm at a dose of 12.5 nC cm^{-1} (Fig. S17†). Notably, when compared to high voltage exposure, the resolution and sensitivity for **Sn4-MB** was significantly improved at low voltage, though the LER exhibited a marginal increase (Fig. S18†).

In high-NA EUV lithography, the increase in NA from 0.33 to 0.55 leads to a substantial reduction in the depth of focus (DoF), as dictated by the Rayleigh criterion. Consequently, it is imperative to correspondingly reduce the thickness of the photoresist film. In this context, 21 nm-thick films were obtained by spin-coating a 5 mg mL^{-1} solution of the **Sn4-MB** photoresist for exposure experiments. Upon development with a mixture of EA and IPA, **Sn4-MB** produced a periodic line with a CD of 17.0 nm at a 40 nm pitch with an exposure dose of 26 nC cm^{-1} (Fig. 3a). Furthermore, when developed solely with EA, **Sn4-MB** achieved CD lines of 20.9 nm at the identical exposure dose (Fig. 3b). Under the 40 nm pitch line mode, the line CDs of 16.4 nm and 19.2 nm were produced at minimum doses of 23 nC cm^{-1} and 15.5 nC cm^{-1}, respectively, by using EA : IPA and EA alone as developers (Fig. S19 and S20†). Thinner **Sn4-MB** films successfully produced L/S patterns with a 40 nm pitch, demonstrating improved CD and line edge roughness (LER) under EA : IPA development, while requiring lower exposure doses for development with EA (Fig. 3c and d).
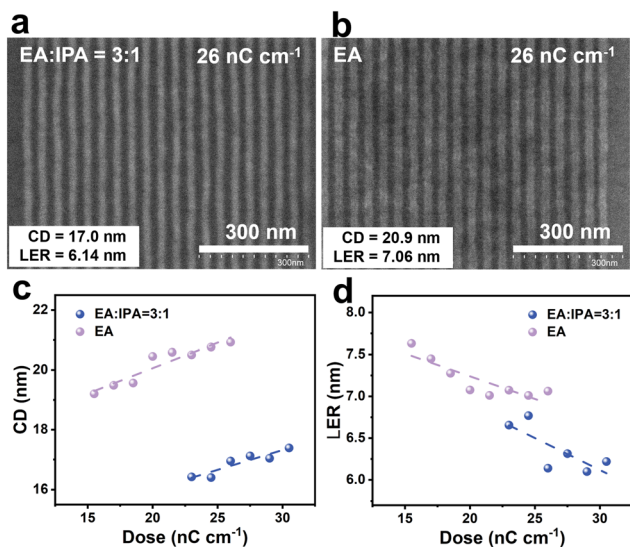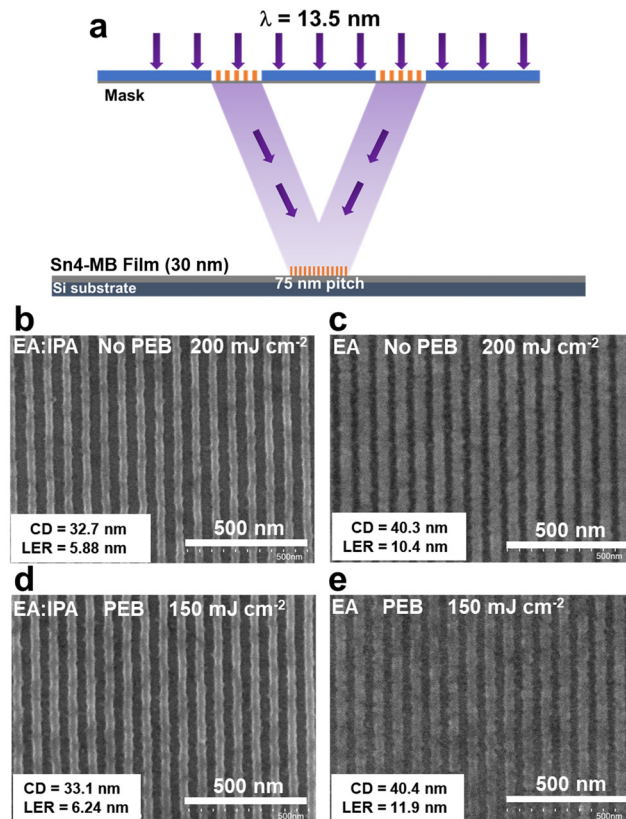

Fig. 4 EUV lithography results of the **Sn4-MB** photoresist obtained at the Shanghai Synchrotron Radiation Facility (SSRF) using a 13.5 nm wavelength and a 75 nm pitch mask. (a) Schematic of the EUV exposure setup. SEM images of **Sn4-MB**'s periodic L/S lines without PEB at an EUV exposure dose of 200 mJ cm^{-2} using (b) EA : IPA = 3 : 1 and (c) EA development; SEM images of **Sn4-MB**'s periodic L/S lines with PEB at a reduced dose of 150 mJ cm^{-2} using (d) EA : IPA = 3 : 1 and (e) EA development.

Fig. 3 SEM images of lines with a period of 40 nm at 26 nC cm^{-1} dose for thinner **Sn4-MB** films developed using (a) EA : IPA = 3 : 1 and (b) EA; relation of 40 nm pitch line (c) CD and (d) LER with dose after EA : IPA = 3 : 1 and EA development of thinner **Sn4-MB** films upon EBL line-exposure.

EUV exposure experiments were performed at the Shanghai Synchrotron Radiation Facility (SSRF) (Fig. 4a).[48] In the absence of post-exposure bake (PEB), under pitch lines of 75 nm and a exposure dose of 200 mJ cm^{-2}, the line CD and LER of 32.7 nm and 5.88 nm were obtained for EA : IPA development, while 40.3 nm and 10.4 nm for EA-alone development (Fig. 4b and c). Conversely, the application of PEB at 100 °C for 1 minute prior to development reduced the required dose to 150 mJ cm^{-2}. In this scenario, the development using EA : IPA resulted in lines with a CD of 33.1 nm and a LER of 6.24 nm (Fig. 4d). Comparably, periodic lines developed only with EA exhibited a CD of 40.4 nm and a LER of 11.9 nm (Fig. 4e). The implementation of PEB did not significantly alter the pattern resolution, but markedly enhanced the sensitivity.

Sn4-MB is not a chemically amplified resist (CAR), but instead operates *via* a photoinduced rearrangement of its metal-oxo cluster network. Upon exposure, ligand cleavage and radical-driven recombination initiate structural reorganization in the exposed areas. The subsequent PEB step facilitates further condensation and crosslinking, which reduces the

© 2025 The Author(s). Co-published by the Institute of Process Engineering, Chinese Academy of Sciences and the Royal Society of Chemistry

Ind. Chem. Mater., 2025, **3**, 543–552 | **547**

solubility of the exposed regions and enhances sensitivity. However, the thermal treatment may also cause slight feature broadening and increased LER due to molecular diffusion and stress relaxation during baking.

Typically, the EUV exposure dose required for Sn12 exceeds 400 mJ cm^{-2}.[28,49] In comparison, **Sn4-MB** achieves a significantly lower dose of 150 mJ cm^{-2} (with PEB), while maintaining high-resolution patterning with CDs around 33 nm. Although differences in testing platforms and process conditions exist, this result demonstrates that **Sn4-MB** operates at a competitive level among state-of-the-art EUV photoresists, validating the effectiveness of our ligand design strategy.

2.2 Composition and structure of the exposure product

Following the assessment of the patterning capabilities of **Sn4-MB**, an investigation was conducted into its variations and underlying mechanisms during exposure. Thermogravimetric analysis coupled with mass spectrometry (TGA-MS) revealed that **Sn4-MB** exhibited thermal stability up to 200 °C. As the temperature increased, a reduction in the weight of **Sn4-MB** was observed. At 500 °C, approximately 15 wt% of **Sn4-MB** remained (Fig. 5a). The mass-to-charge ratios (m/z) detected at 16 and 56

were identified as CH_4 and C_4H_8, respectively, which originated from the thermally induced cleavage of Sn–methyl and Sn–butyl bonds in **Sn4-MB**. Additionally, the peaks observed at $m/z = 136$ and 44 were attributed to adamantane and CO_2, indicating the decarboxylation of adamantane carboxylic acids.

X-ray photoelectron spectroscopy (XPS) was employed to examine the changes in **Sn4-MB** under X-ray irradiation. Following one hour of X-ray irradiation, the relative concentrations of both the carbon (C) and oxygen (O) elements diminished (Fig. 5b), which can be attributed to the dissociation of organic ligands and the decarboxylation process (Table S1†). The C 1s XPS spectra of the **Sn4-MB** film were analyzed and fitted both prior to and following irradiation, with binding energies of $E_b = 284.8$ eV (indicated in green), 286.2 eV (indicated in purple), and 288.6 eV (indicated in yellow). These energies correspond to aliphatic carbon (C–H), Sn–C bonds, and carbonyl carbon (C=O), respectively (Fig. 5b). The observed decrease in the relative content of C–H from 12.8% to 8.54%, alongside the increase in the relative content of Sn–C from 1.93% to 2.19%, provides evidence for the cleavage and rearrangement of Sn–alkyl bonds, resulting in the formation of new Sn–C bonds derived from both Sn–alkane–Sn and Sn–adamantane–Sn linkages. In the case of the O 1s XPS, two peaks
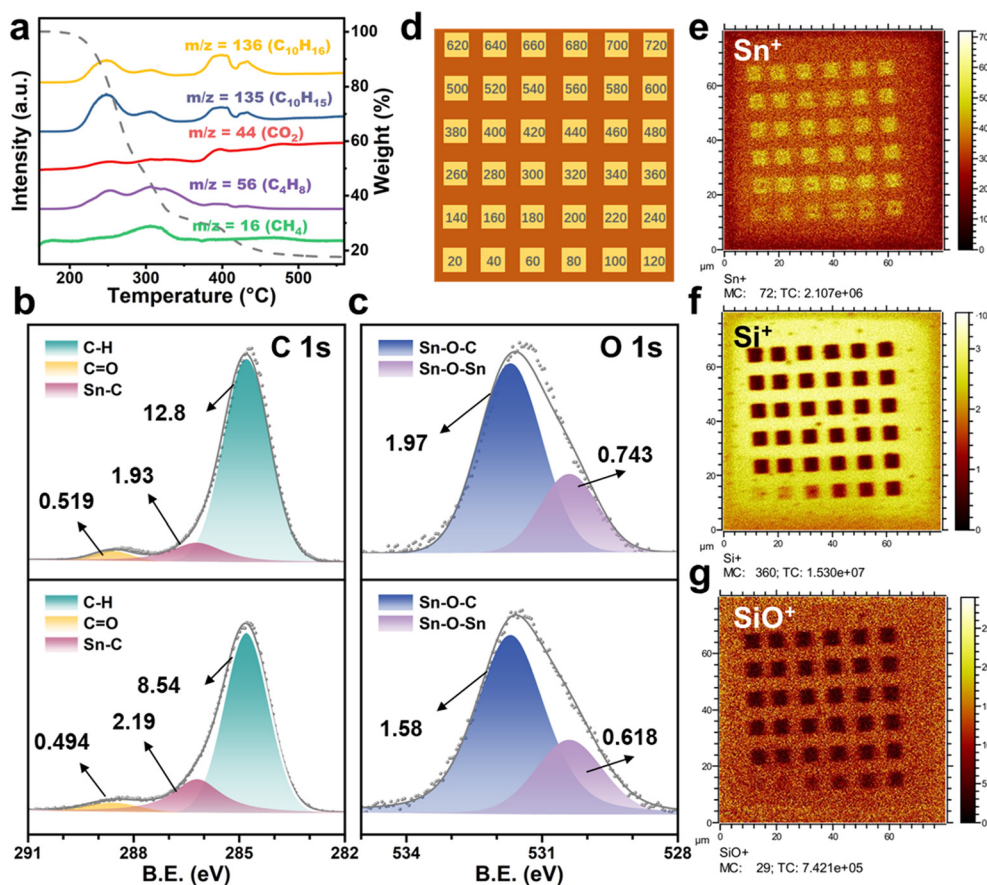

Fig. 5 (a) TGA-MS curves of **Sn4-MB**, the grey dashed line is the change in sample mass as a function of temperature; XPS for (b) C 1s and (c) O 1s XPS spectra of **Sn4-MB** after 1 hour X-ray exposure; (d) schematic illustration of the exposure dose distribution (values in μC cm^{-2}); surface ToF-SIMS images of exposed **Sn4-MB** films showing (e) Sn$^+$, (f) Si$^+$ (g) and SiO$^+$ distributions.

were fitted at E_b = 531.7 eV (depicted in blue) for Sn–O–C and E_b = 530.4 eV (depicted in light purple) for Sn–O–Sn (Fig. 5c). The reduction in the relative content of Sn–O–C further corroborates the occurrence of decarboxylation of the adamantane carboxylic acid.

To obtain further insights into the exposure products, time-of-flight secondary ion mass spectrometry (ToF-SIMS) was conducted on **Sn4-MB**.[50,51] The mass spectrometry results indicated that the m/z values of 154.86 and 163.86 for the exposed **Sn4-MB** films corresponded to $Sn^+(CH_2)_5Sn^+$ and Sn^+-$H_2(CH_2)_6Sn^+H_2$, respectively, suggesting that SnO_x nuclei were interconnected by alkyl chains. Additionally, the m/z values of 194.88 and 254.97 were attributed to $Sn^+H_2(C_{10}H_{14})CH_2Sn^+H_2$ and $Sn^+C_{10}H_{15}$, respectively, confirming that adamantyl radicals generated through decarboxylation also contributed to the linkage of the SnO_x nuclei (Fig. S21†). Two-dimensional mapping images of Sn^+ and Si^+ in **Sn4-MB** films following array exposure were analyzed (Fig. 5d). As the exposure dose increased from 20 μC cm^{-2} to 120 μC cm^{-2}, the Sn^+ signal in the exposure area exhibited a corresponding increase; however, the Sn^+ signal remained relatively constant at higher doses (Fig. 5e). Conversely, the Si^+ and SiO^+ signals diminished with increasing exposure dose, demonstrating an inverse relationship to the Sn^+ signal (Fig. 5f and g). This phenomenon can be attributed to the fact that, with an increase in exposure dose, a greater number of Sn atoms participated in the photolithographic reaction, resulting in the formation of metal–organic polymers that were insoluble in the developer. Consequently, these polymers remained on the film after development, leading to a thickness of the retained photoresist that rendered the Si^+ and SiO^+ in the substrate undetectable.

According to the experimental results of TGA-MS, XPS, and ToF-SIMS, the Sn–methyl and Sn–butyl bonds, along with the radicals generated in **Sn4-MB**, participate in an intramolecular feedback regulation mechanism (Fig. 6). Due to the lower bond dissociation energy of Sn–butyl compared to Sn–methyl (Fig. S10†), the butyl groups are more susceptible to cleavage upon exposure, generating active butyl radicals. This cleavage process directly initiated the photolithographic reaction involving the intramolecular Sn–methyl. These radicals initiate a broader reaction diffusion process, which can compromise resolution if left uncontrolled. However, within **Sn4-MB**, the initially

generated butyl radicals can induce the formation of highly reactive and short-lived methyl radicals from Sn–methyl groups. These methyl radicals are capable of quenching excess butyl radicals, thereby suppressing their over-diffusion and confining the reaction zone.

In contrast to the intermolecular interactions observed between Sn4–Me–C10 and Sn4–Bu–C10 in the hybrid photoresist formulation, the intramolecular interactions between Sn–methyl and Sn–butyl in **Sn4-MB**, facilitated by the mutual feedback regulation of free radicals, reduced energy transfer losses and suppressed the extent of reaction diffusion. This mechanism resembles the resolution enhancement strategy observed in chemically amplified resists (CARs), where covalent bonding of photoacid generators to the polymer backbone enables more effective control of acid diffusion. Similarly, the intramolecular hybridization strategy employed in **Sn4-MB** offers superior suppression of reaction diffusion compared to physically mixed systems. As a result, the patterning properties of **Sn4-MB** exhibited significant and comprehensive improvements when compared to those of hybrid photoresist formulations.

2.3 Etch resistance

The observed slower etching rate and enhanced etching selectivity between the substrate and photoresist films suggest a seamless transfer of micro- and nanopatterns. Consequently, the etching rate of **Sn4-MB** was evaluated under conditions of deep silicon etching. Prior to the etching process, the height of the **Sn4-MB** line was measured at 27.3 nm. Following 20 seconds of etching, the line height increased to 83.3 nm, while the etching rate of the silicon substrate was determined to be 3.94 nm s^{-1} (Fig. S22†). Thus, the calculated etching rate for **Sn4-MB** was found to be 1.14 nm s^{-1}, resulting in an etching selectivity ratio of approximately 3.45 : 1 relative to the silicon substrate.

3 Conclusions

In this study, a hybrid alkyl TOCs EUV photoresist, designated as **Sn4-MB**, was synthesized and evaluated for its patterning properties. The significant and comprehensive enhancement of the patterning capacity of **Sn4-MB**, in comparison to the hybrid
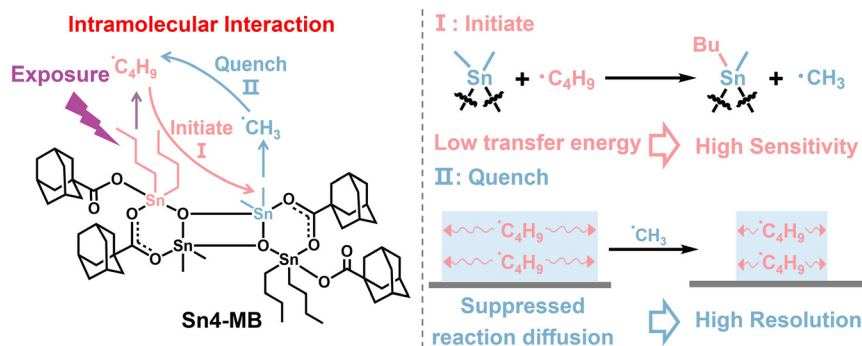

Fig. 6 Schematic exposure mechanism of **Sn4-MB** photoresist formulations.

photoresist formulation, can be attributed to the intramolecular interactions between Sn–methyl and Sn–butyl bonds, as well as the generated radicals. These interactions effectively reduce energy transfer losses and suppress the extent of reaction diffusion. Through the optimization of the developer, low-voltage EBL exposure, and a reduction in photoresist film thickness, the patterning capability of **Sn4-MB** was further improved, achieving 40 nm pitch periodic lines with a CD of 16.3 nm. Under EUV exposure, **Sn4-MB** successfully produced 75 nm pitch lines with a CD of 33.1 nm at an exposure dose of 150 mJ cm^{-2}. This study presents an effective molecular design strategy for enhancing the performance of TOC EUV photoresists and may serve as an inspiration for the development of other novel metal oxide materials.

4 Experimental section

4.1 Spin-coating procedures

10 mg of **Sn4-MB** was dissolved in 1 mL of chloroform and subjected to sonication for 10 minutes. The resulting solution was purified twice using a 0.22 μm PTFE needle filter and was subsequently spin-coated onto polished wafers measuring 1 cm^2 at a speed of 6000 rpm for 30 seconds. Following this, the coated wafers were baked at 70 °C for 1 minute in ambient air. To achieve thinner **Sn4-MB** films, precursor solutions with concentrations of 3 mg mL^{-1}, 5 mg mL^{-1}, and 8 mg mL^{-1} were prepared using the same methodology, and the corresponding films were produced at spin-coating speeds of 6000 rpm, 7000 rpm, and 8000 rpm, respectively.

4.2 Line space pattern

Sn4-MB films were subjected to electron beam lithography (EBL) line exposure experiments utilizing Raith's ELPHY nanopatterning generator. Initial exposure experiments on the **Sn4-MB** films were conducted at an accelerating voltage of 30 kV, employing template lines with periods of 100 nm and 70 nm, and doses ranging from 0.5 to 30.5 nC cm^{-1}. Following exposure, the samples underwent a post-exposure bake (PEB) for 1 minute at 100 °C, after which they were developed in a solution of isopropyl alcohol (IPA) and deionized water (DIW) in a 3 : 1 ratio for 20 seconds. This was followed by a rinse in DIW for 5 seconds and a hard bake at 100 °C for 1 minute. Alternatively, the exposed **Sn4-MB** film samples were developed directly using a mixture of ethyl acetate (EA) and IPA in a 3 : 1 ratio or with EA alone. Subsequently, the same EBL exposure experiment was repeated at an accelerating voltage of 10 kV, with a template line period of 70 nm. Additionally, **Sn4-MB** films that were spin-coated with a precursor solution at a concentration of 5 mg mL^{-1} were tested in EBL exposure experiments at an accelerating voltage of 30 kV, utilizing a line template period of 40 nm. The patterned lines were subsequently analyzed using scanning electron microscopy (SEM), and the critical dimensions (CD) and line edge roughness (LER) of the lines were quantified using the SMILE software.[52,53] The profiles of the patterned lines were measured using atomic force microscopy (AFM) and transmission electron microscopy (TEM) under the scanning transmission electron microscopy (STEM) model.

Data availability

The data supporting this article have been included as part of the ESI.†

Author contributions

Hao Chen was responsible for the synthesis of photoresist materials, the design of experiments, and the drafting of the manuscript. Wenzheng Li organized the data and contributed to the writing and editing of the manuscript. Yingdong Zhao assisted in refining the manuscript and provided support in SEM imaging. Xinyan Huang and Peijun Ji participated in the EBL experiments. Jun Zhao offered guidance for the EUVL experiments. Jialong Zhang provided financial support. Pengzhong Chen and Xiaojun Peng provided financial support, supervised the experiments and revised the manuscript.

Conflicts of interest

The authors declare no conflict of interest.

Acknowledgements

References

1 Y. Qie, H. Hu, K. Yu, C. Zhong, S. Ju, Y. Liu, T. Guo and F. Li, Ligand-nondestructive direct photolithography assisted by semiconductor polymer cross-linking for high-resolution quantum dot light-emitting diodes, *Nano Lett.*, 2024, **24**, 1254–1260.

2 S. Wei, J. Yuan, G. Yang, H. Zhong, Y. Dong and J. Shi, A photoinitiator-grafted photoresist for direct in situ lithography of perovskite quantum dots, *ACS Appl. Nano Mater.*, 2024, **7**, 26397–26404.

3 M. G. Kim, D. K. Brown and O. Brand, Nanofabrication for all-soft and high-density electronic devices based on liquid metal, *Nat. Commun.*, 2020, **11**, 1002.

4 Q. Wang, Y. Zhou, X. Wang, H. Gao, Z. Shu, Z. Hu, P. Tao, Y. Ekinci, M. Vockenhuber, Y. Chen, H. Duan, H. Xu and X. He, Suppressing of secondary electron diffusion for high-precision nanofabrication, *Mater. Today*, 2023, **67**, 95–105.

5 C. Luo, C. Xu, L. Lv, H. Li, X. Huang and W. Liu, Review of recent advances in inorganic photoresists, *RSC Adv.*, 2020, **10**, 8385–8395.

6 B. Wu and A. Kumar, Extreme ultraviolet lithography and three dimensional integrated circuit—a review, *Appl. Phys. Rev.*, 2014, **1**, 011104.

7 X. Wang, P. Tao, Q. Wang, R. Zhao, T. Liu, Y. Hu, Z. Hu, Y. Wang, J. Wang, Y. Tang, H. Xu and X. He, Trends in photoresist materials for extreme ultraviolet lithography: A review, *Mater. Today*, 2023, **67**, 299–319.

8 J. Chen, Q. Hao, S. Wang, S. Li, T. Yu, Y. Zeng, J. Zhao, S. Yang, Y. Wu, C. Xue, G. Yang and Y. Li, Molecular glass resists based on 9,9′-spirobifluorene derivatives: Pendant effect and comprehensive evaluation in extreme ultraviolet lithography, *ACS Appl. Polym. Mater.*, 2019, **1**, 526–534.

9 W. T. James, Materials challenges for sub-20-nm lithography, *J. Micro/Nanolithogr., MEMS, MOEMS*, 2011, **10**, 033009.

10 C. Wagner and N. Harned, Lithography gets extreme, *Nat. Photonics*, 2010, **4**, 24–26.

11 Z. Tang, X. Guo, H. Wang, H. Chen and W. Kang, A new metallization method of modified tannic acid photoresist patterning, *Ind. Chem. Mater.*, 2024, **2**, 284–288.

12 Z. Wang, J. Chen, T. Yu, Y. Zeng, X. Guo, S. Wang, T. Allenet, M. Vockenhuber, Y. Ekinci, G. Yang and Y. Li, Sulfonium-functionalized polystyrene-based nonchemically amplified resists enabling sub-13 nm nanolithography, *ACS Appl. Mater. Interfaces*, 2023, **15**, 2289–2300.

13 H. An, J. Chen, Y. Zeng, T. Yu, S. Wang, X. Guo, R. Hu, P. Tian, M. Vockenhuber, D. Kazazis, Y. Ekinci, G. Yang and Y. Li, Increasing the sensitivity of nonchemically amplified resists by oxime sulfonate-functionalized polystyrene, *ACS Appl. Polym. Mater.*, 2024, **6**, 5374–5384.

14 N. Fu, Y. Liu, X. Ma and Z. Chen, EUV lithography: State-of-the-art review, *J. Microelectron. Manuf.*, 2019, **2**, 14.

15 P. Alberto, S. Jan van, T. Kars, B. Rob van, K. Peter, S. Judon, L. Erik, B. Jos, F. Jo, M. Hans, S. Eelco van, M. Niclas, D. Jeannot, S. Uwe, K. Bernhard, T. Bernd, K. Winfried, H. Tilmann and M. Sascha, The future of EUV lithography: Enabling moore's law in the next decade, *Proc. SPIE*, 2017, **10143**, 101430G.

16 O. O. Versolato, J. Sheil, S. Witte, W. Ubachs and R. Hoekstra, Microdroplet-tin plasma sources of EUV radiation driven by solid-state-lasers (topical review), *J. Opt.*, 2022, **24**, 054014.

17 C. K. Ober, F. Käfer and C. Yuan, Recent developments in photoresists for extreme-ultraviolet lithography, *Polymer*, 2023, **280**, 126020.

18 S. Fujii, T. Kozawa, K. Okamoto, J. J. Santillan and T. Itani, Shot noise limit of sensitivity of chemically amplified resists used for extreme ultraviolet lithography, *Jpn. J. Appl. Phys.*, 2015, **54**, 116501.

19 R. Kumar, M. Chauhan, M. G. Moinuddin, S. K. Sharma and K. E. Gonsalves, Development of nickel-based negative tone metal oxide cluster resists for sub-10 nm electron beam and helium ion beam lithography, *ACS Appl. Mater. Interfaces*, 2020, **12**, 19616–19624.

20 N. Thakur, M. Vockenhuber, Y. Ekinci, B. Watts, A. Giglia, N. Mahne, S. Nannarone, S. Castellanos and A. M. Brouwer, Fluorine-rich zinc oxoclusters as extreme ultraviolet photoresists: Chemical reactions and lithography performance, *ACS Mater. Au*, 2022, **2**, 343–355.

21 G. Lim, K. Lee, S. Choi and H. J. Yoon, Organometallic and coordinative photoresist materials for EUV lithography and related photolytic mechanisms, *Coord. Chem. Rev.*, 2023, **493**, 215307.

22 D. Wang, R. Xu, D. Zhou, J. Zhao, J. Zhang, P. Chen and X. Peng, Zn-ti oxo cluster photoresists for EUV lithography: Cluster structure and lithographic performance, *Chem. Eng. J.*, 2024, **493**, 152315.

23 L. Wu, M. F. Hilbers, O. Lugier, N. Thakur, M. Vockenhuber, Y. Ekinci, A. M. Brouwer and S. Castellanos, Fluorescent labeling to investigate nanopatterning processes in extreme ultraviolet lithography, *ACS Appl. Mater. Interfaces*, 2021, **13**, 51790–51798.

24 Q. Wang, H. Cui, X. Wang, Z. Hu, P. Tao, M. Li, J. Wang, Y. Tang, H. Xu and X. He, Exceptional light sensitivity by thiol-ene click lithography, *J. Am. Chem. Soc.*, 2023, **145**, 3064–3074.

25 Y. Zhao, X. Huang, Y. Si, L. Zheng, H. Chen, J. Zhao, F. Luo, J. Zhang, P. Chen and X. Peng, Additive-assisted forming high-quality thin films of Sn-oxo cluster for nanopatterning, *ACS Appl. Mater. Interfaces*, 2024, **16**, 41659–41668.

26 F.-F. Liu, G.-Y. Shi, N. Zhen, Z.-H. Zhou, T.-L. Guo, Y. Qiao, J. Zhao, J.-C. Liu, F. Luo and L. Zhang, Single rare-earth ion doped tin-oxo nanocluster photoresists for high-resolution extreme ultraviolet lithography, *Nano Lett.*, 2025, **25**, 2067–2073.

27 D. Wang, X. Yi and L. Zhang, Non-alkyl tin-oxo clusters as new-type patterning materials for nanolithography, *Sci. China:Chem.*, 2022, **65**, 114–119.

28 B. Cardineau, R. Del Re, M. Marnell, H. Al-Mashat, M. Vockenhuber, Y. Ekinci, C. Sarma, D. A. Freedman and R. L. Brainard, Photolithographic properties of tin-oxo clusters using extreme ultraviolet light (13.5nm), *Microelectron. Eng.*, 2014, **127**, 44–50.

29 J. Shi, A. Ravi, N. E. Richey, H. Gong and S. F. Bent, Molecular layer deposition of a hafnium-based hybrid thin film as an electron beam resist, *ACS Appl. Mater. Interfaces*, 2022, **14**, 27140–27148.

30 F. Roberto, H. Jarich, W. Lianjia, O. Sonia Castellanos, M. B. Albert and E. Yasin, Absorption coefficient of metal-containing photoresists in the extreme ultraviolet, *J. Micro/Nanolithogr., MEMS, MOEMS*, 2018, **17**, 023505.

31 T. Manouras and P. Argitis, High sensitivity resists for EUV lithography: A review of material design strategies and performance results, *Nanomaterials*, 2020, **10**, 1593.

32 Y. Peng, P. Chen, H. Chen, Y. Si and X. Peng, Absorption-coefficient calculation of short-wavelength photoresist materials: From EUV to BEUV and water window x-ray, *Smart Mol.*, 2024, e20240043.

33 Y. Si, Y. Zhao, G. Shi, D. Zhou, F. Luo, P. Chen, J. Fan and X. Peng, A novel stable zinc-oxo cluster for advanced

© 2025 The Author(s). Co-published by the Institute of Process Engineering, Chinese Academy of Sciences and the Royal Society of Chemistry

Ind. Chem. Mater., 2025, **3**, 543–552 | **551**

lithography patterning, *J. Mater. Chem. A*, 2023, **11**, 4801–4807.

34 H. Chen, X. Huang, Y. Zhao, J. Zhao, P. Chen and X. Peng, Balancing sensitivity and resolution by feedback regulation of free radicals from Sn-C bonds in tin-oxygen clusters ebl photoresist, *Sci. China Mater.*, 2024, **67**, 3142–3150.

35 H. Chen, Y. Peng, H. Fu, F. Han, G. Shi, F. Luo, J. Zhao, D. Zhou, P. Chen and X. Peng, Effect of free radicals on irradiation chemistry of a double-coordination organotin (Sn4) photoresist by adjusting alkyl ligands, *CCS Chem.*, 2024, **6**, 2044–2053.

36 H. Jarich, Z. Yu, V. Michaela, K. Dimitrios, E. Yasin and M. B. Albert, Extreme ultraviolet patterning of tin-oxo cages, *J. Micro/Nanolithogr., MEMS, MOEMS*, 2017, **16**, 033510.

37 N. Thakur, R. Bliem, I. Mochi, M. Vockenhuber, Y. Ekinci and S. Castellanos, Mixed-ligand zinc-oxoclusters: Efficient chemistry for high resolution nanolithography, *J. Mater. Chem. C*, 2020, **8**, 14499–14506.

38 H. Xu, K. Sakai, K. Kasahara, V. Kosma, K. Yang, H. C. Herbol, J. Odent, P. Clancy, E. P. Giannelis and C. K. Ober, Metal-organic framework-inspired metal-containing clusters for high-resolution patterning, *Chem. Mater.*, 2018, **30**, 4124–4133.

39 R. Ryan Del, S. Miriam, P. James, C. Brian, E. Yasin, V. Michaela, N. Mark, F. Daniel and L. B. Robert, Low-ler tin carboxylate photoresists using EUV, *Proc. SPIE*, 2015, **9422**, 942221.

40 Y. Si, D. Zhou, J. Zhao, Y. Peng, P. Chen, J. Fan and X. Peng, Radiation chemistry of a novel zinc-oxo cluster crosslinking strategy for EUV patterning, *Sci. China Mater.*, 2024, **67**, 1588–1593.

41 R. Fallica, N. Mahne, T. Conard, A. Vanleenhove, D. de Simone and S. Nannarone, Mean free path of electrons in organic photoresists for extreme ultraviolet lithography in the kinetic energy range 20-450 ev, *ACS Appl. Mater. Interfaces*, 2023, **15**, 35483–35494.

42 J. Y. Park, H.-J. Song, T. C. Nguyen, W.-J. Son, D. Kim, G. Song, S.-K. Hong, H. Go, C. Park, I. Jang and D. S. Kim, Novel mechanism-based descriptors for extreme ultraviolet-induced photoacid generation: Key factors affecting extreme ultraviolet sensitivity, *Molecules*, 2023, **28**, 6244.

43 K. Jake, G. Steven, G. Sean, C. Jonathan, W. Ulrich, S. M. Lawrence, III, K. Yudhishthir, L. B. Robert and D. Greg, Investigating the threshold electron energy for reactions in EUV resist materials, *Proc. SPIE*, 2018, **10586**, 105861N.

44 Y. Zhang, J. Haitjema, M. Baljozovic, M. Vockenhuber, D. Kazazis, T. A. Jung, Y. Ekinci and A. M. Brouwer, Dual-tone application of a tin-oxo cage photoresist under e-beam and EUV exposure, *J. Photopolym. Sci. Technol.*, 2018, **31**, 249–255.

45 N. Sadegh, M. van der Geest, J. Haitjema, F. Campi, S. Castellanos, P. M. Kraus and A. M. Brouwer, Xuv induced bleaching of a tin oxo cage photoresist studied by high harmonic absorption spectroscopy, *J. Photopolym. Sci. Technol.*, 2020, **33**, 145–151.

46 A. Sasaki, M. Ishino and M. Nishikino, An estimation of line width roughness of photoresists due to photon shot noise for extreme ultraviolet lithography using the percolation model, *Jpn. J. Appl. Phys.*, 2019, **58**, 055002.

47 W. Thomas, H. Craig, B. Robert, P. Karen, M. Warren, K. Chiew-Seng, D. Greg, W. Obert and W. Yayi, Evaluation of EUV resist materials for use at the 32 nm half-pitch node, *Proc. SPIE*, 2008, **6921**, 69211F.

48 Z.-J. Li, C.-H. Qi, B.-N. Li, S.-M. Yang, J. Zhao, Z.-D. Lei, S.-J. Zhu, H. Shi, L. Wang, Y.-Q. Wu and R.-Z. Tai, Latest developments in EUV photoresist evaluation capability at shanghai synchrotron radiation facility, *Nucl. Sci. Tech.*, 2023, **34**, 198.

49 Y. K. Kang, H. Kim, S. J. Lee, D.-S. Oh, Y.-H. Yoon, C.-J. Kim, G. Y. Yeom, C.-C. Hwang and M.-G. Kim, Enhancement of photosensitivity and stability of Sn-12 EUV resist by integrating photoactive nitrate anion, *Appl. Surf. Sci.*, 2024, **656**, 159564.

50 S. Ravati, S. Poulin, K. Piyakis and B. D. Favis, Phase identification and interfacial transitions in ternary polymer blends by tof-sims, *Polymer*, 2014, **55**, 6110–6123.

51 C. M. Chan and L. T. Weng, Surface characterization of polymer blends by xps and tof-sims, *Materials*, 2016, **9**, 655.

52 M. Iacopo, V. Michaela, A. Timothée and E. Yasin, Contacts and lines sem image metrology with smile, *Proc. SPIE*, 2021, **11855**, 1185502.

53 M. Iacopo, V. Michaela, A. Timothée and E. Yasin, Open-source software for sem metrology, *Proc. SPIE*, 2020, **11518**, 115180G.